# Microstructure and properties of C/C–ZrC composites prepared by hydrothermal deposition combined with carbothermal reduction

Li Cuiyan*[1], Li Guibiao[1], Ouyang Haibo*[1], Huang Jianfeng[1], Hou Xianghui[2]

1 School of Materials Science & Engineering, Shaanxi University of Science & Technology, Xi'an, Shaanxi, 710021, China

2 Faculty of Engineering, The University of Nottingham, Nottingham NG7 2RD, UK

**Abstract**

Carbon fiber reinforced carbon matrix containing ZrC (C/C–ZrC) composites were prepared by hydrothermal deposition combined with carbothermal reduction. The submicron ZrC particles (100~300 nm) were dispersed in the matrix. The stress-strain curves of the composites presented a typical pseudo-plastic fracture behavior. The mass and linear ablation rates of the composites were $3.7\times10^{-3}$ g/s and $4.2\times10^{-3}$ mm/s, respectively. The formation of $ZrO_2$ glass layer reduced erosion of the composites in the ablation center. The continuous C–ZrC–$ZrO_2$ skeleton layer generated from the oxidation of ZrC can protect the composites from erosion at the ablation brim region. The obtained C/C–ZrC composites present a promising potential as ablation resistance materials.

Keywords: C/C–ZrC composites; hydrothermal deposition; microstructure; ablation resistance;

## 1. Introduction

Carbon fiber reinforced carbon matrix containing ultra-high temperature ceramic

* Corresponding author. Tel./fax: +86 029 86168802.

E-mail addresses: licuiyan@sust.edu.cn (Li C.Y.), ouyangsust@126.com (Ouyang H.B.)

(C/C–UHTCs) composites present a promising application as high temperature structural components for space vehicles, such as nose tips, leading edges, and nozzles, due to their excellent high temperature mechanical properties, good thermal shock resistance and ablation resistance [1,2]. To date, various techniques have been used to prepare the C/C–UHTCs composites, such as precursor infiltration and pyrolysis (PIP) process [3], reactive melt infiltration (RMI) [4,5], solution infiltration [6,7], and powder slurry infiltration [8,9]. As a current popular method, PIP can prepare the C/C–UHTCs composites with uniform distribution of UHTCs particles [10-12]. However, for the PIP method, the synthesis of the UHTCs precursor is complicated and the ceramic yield of the precursor is low in the pyrolysis process, which results in a high cost for the fabrication of the C/C–UHTCs composites.

Recently, Lu et al. [13] proposed to deposit the ZrC precursors in the carbon fiber preform by chemical liquid-vapor deposition (CLVD) process. After that, the C/C–ZrC composites were prepared by heat treatment and isothermal chemical vapor infiltration (ICVI) densification. Results showed that the pyrolytic carbon and ceramics were co-deposited on the carbon fibers. The C/C–ZrC composites exhibited excellent ablation resistance and a brittle fracture behavior due to relatively strong interfacial bonding strength between fibers and matrix. In addition, a joint methods of CLVD and PIP for the fabrication of C/C–ZrC composites was reported to improve the fully and homogeneously infiltrate of the composites [14]. Our previous work [15] introduced ZrC precursors into the carbon fibers preforms by the microwave hydrothermal process. The C/C–ZrC composites were prepared by subsequent the thermal gradient chemical vapor infiltration (TCVI) and carbothermal reduction. Results showed that submicron ZrC particles homogeneously dispersed in the carbon matrix, which is helpful to form a continuously melting $ZrO_2$ layer and can prevent

carbon from oxidation and restrain the mechanical erosion of the composites.

Up to the present, the carbon matrix of the composite was mainly pyrolytic carbon generated from ICVI or TCVI process. Biomass as carbon sources for the preparation of carbonaceous materials, such as carbon microspheres and carbon materials with nanostructure has also been studied. The C/C composites fabricated by hydrothermal carbonization using starch as the carbon source, indicating that using biomass as precursors for the densification of C/C composites is feasible [16]. Cao et al. [17] reported that $C_f$/C–SiC–$MoSi_2$ composites were fabricated by a two-step hydrothermal treatment. SiC and $MoSi_2$ ceramics were first infiltrated into porous C/C composites by a hydrothermal step. Then, the samples contained ceramics was densified by a second hydrothermal process using glucose as carbon source. The good ablation behavior was attributed to the higher density of the ceramics, and the generation of $SiO_2$ and $MoO_2$. However, the inhomogeneity distribution of ceramic particles in the composites restricted further improvement of the ablation resistance.

Hydrothermal technology is a common method for the preparation oxide nanoparticles [18,19]. The UHTCs can be prepared by the reaction of the oxide nanoparticles with carbon at high temperature [20,21]. In this study, we proposed a novel method to prepare C/C–ZrC composites containing sub-micron scale ZrC particles. The matrix of the composites, that is, C–ZrC matrix was formed by repeated alternating hydrothermal deposition combined with the carbothermal reduction. The microstructure and mechanical properties of the C/C–ZrC composites were studied. The ablation resistance and mechanism of the composites were also investigated.

## 2. Experimental

### 2.1 Fabrication of composites

Needled carbon fiber felts with a density of 0.40 g/cm$^3$ (Yixing Tianniao High

Technology Co., Ltd, Jiangsu, China) fabricated by alternatively stacked non-woven layers and short-cut fiber webs by a needle-punching technique, were used as reinforcement of the composites. Sucrose (Chemically Pure, Aladdin Industrial Corporation) was employed as the carbon source. Zirconium tetrachloride ($ZrCl_4$, analytical grade, Sinopharm Chemical Reagent Co., Ltd, Shanghai, China) was used as $ZrO_2$ precursor.

Fig. 1 shows the schematic for the preparation of the C/C–ZrC composites. Sucrose was dissolved in water with a concentration of 200 g/L. The carbon felts and 60 ml sucrose solution were put into a Teflon autoclave. The hydrothermal reaction was performed in a microwave accelerated reaction system (MARS-10, Sineo Microwave) for 120 min at 180 °C. And then the carbon fiber felts were dried at 80 °C for 2 hours. $ZrCl_4$ was dissolved in deionized water, and the concentration of zirconium ion was set to 0.5 m/L. pH value of the solution was set to 9 using 2 m/L sodium hydroxide solution. The prepared solution and the treated carbon fiber felts were transferred to a Teflon autoclave. Hydrothermal deposition was performed in the aforementioned reaction system for 30 min at 200 °C. The treated carbon fiber preforms were washed by water to get rid of the $Na^+$ and then dried at 80 °C for 2 hours. The hydrothermal deposition of carbon and $ZrO_2$ was carried out for 10 cycles to get the densified C/C–$ZrO_2$ composites, which were treated at 1,500 °C for 2 h in an argon atmosphere. The density and open porosity of the composites were 1.68±0.05 g/cm$^3$ and 11.4±0.1%, respectively.

2.2 Tests and characterization

The phase composition of the composites was investigated by X-ray diffraction (XRD, X'Pert Pro MPD). The microstructure of the composites was investigated by scanning electron microscopy (SEM, JEOL6390) combined with energy dispersive

spectroscopy (EDS). Raman spectra were collected from the composites at 300–3500 $cm^{-1}$ by Raman Microscope (Renishaw, London, England). Three-point bending test was carried out on the electron universal testing machine (CSS-1110). Specimens dimension was 55×10×4 mm. Specimens were tested with a speed of 0.5 mm/min at room temperature. The loading direction was perpendicular to laminated carbon fiber layers. Four samples were used to evaluate the flexural strength of the composites. The ablation of the C/C–ZrC composites was performed using an oxyacetylene torch for the plate specimens (Φ30×10 mm). The flame temperature was around 3000 °C. The specimens were exposed to the flame for 60 s. The details of ablation parameters were set as previously reported [22].

## 3. Results and discussion

### 3.1 Microstructure of the prepared C/C–ZrC composites

Fig.2 (a) shows SEM morphology of C/C porous sample. Carbon microspheres was formed and deposited on the surface of the carbon fibers after the hydrothermal deposition. Thus, the carbon generated on the carbon fibers, which will provide the carbon source and protect carbon fibers from damaging during the formation of ZrC by carbothermal reduction. Fig. 2(b) presents Raman spectrum of the carbon matrix in C/C porous sample. The Raman spectrum shows two wide bands at 1350 and 1580 $cm^{-1}$, indicating that the carbon matrix is mostly composed of amorphous structure [16, 23]. The amorphous carbon matrix prepared by hydrothermal deposition was used as carbon source to react with $ZrO_2$ during carbothermal reduction, which was expected to form C–ZrC matrix.

The XRD pattern of the prepared C/C–ZrC composites is shown in Fig. 3(a). The C/C–ZrC composites are composed of carbon and ZrC, indicating that amorphous carbon and deposited $ZrO_2$ have reacted and converted to ZrC after heat treatment

(Reaction (1)). The carbothermal reduction of $ZrO_2$ and carbon lead to the shrinkage of the matrix and form lots of closed pores, which might lead to low density of the C/C–ZrC composites (1.68 g/cm$^3$).

$$C + ZrO_2 \rightarrow ZrC + CO \qquad \text{Reaction (1)}$$

Fig. 3(b) shows backscattered electron image of the cross section of C/C–ZrC composites. White spots are found in the matrix of the composites, which are ZrC particles. This phenomenon indicates that $Zr^{4+}$ precursor solution can adequately infiltrated into the fiber webs and nonwoven layer under hydrothermal condition. Obviously, ZrC particles were enriched in fiber webs. During hydrothermal deposition, more $ZrO_2$ particles was deposited in the fiber webs as the spaces in fiber webs were larger than that in nonwoven layer.

Fig.4 (a) shows the SEM morphology of nonwoven layer in the C/C–ZrC composites. The space among fibers was fully filled with matrix materials. Fig.4 (b) presents the magnified micrographs of $90^o$ nonwoven layer (area 1). The C–ZrC matrix fills the space among the carbon fibers and forms a dense matrix surrounding carbon fibers. BSE image further indicated that many ZrC particles uniformly distribute in the matrix of the C/C–ZrC composite ( Fig. 4(c)). Fig. 4(d) is the magnified micrographs of area 2. A carbon layer can be found on the carbon fiber, resulting from the carbon formed by hydrothermal deposition. A large amount of ZrC particles are formed on the surface of the carbon layer, further confirming the uniform distribution of ZrC surrounding carbon fiber in the matrix. In addition, no obvious crack can be found at the interface between the carbon fiber and the C–ZrC matrix. The dimension of ZrC particles in the matrix is 100~300 nm, as shown in Fig. 4(e). It is indicated that carbothermal reduction of hydrothermal deposition carbon and $ZrO_2$ can form sub-micro ZrC particles. The magnified micrograph of $0^o$ nonwoven layer

(as pointed by arrows in Fig.4 (a)) display a gathered microspheres structure with many ZrC particles on carbon fiber surface (Fig.4 (f)). These gathered microspheres is relate to the deposited carbon microspheres on the carbon fiber surface. Fig.4 (g) shows the SEM morphology of fiber webs in the composites. A large amount of ZrC particles filled the spaces among fibers. A carbon layer can also be found on the fiber surfaces shown in Fig.4 (h). These results indicated that sucrose and $Zr^{4+}$ precursor solution can adequately infiltrated into the carbon fiber felts both in nonwoven layer and fiber webs under hydrothermal condition, and then ZrC matrix is formed by the reaction of carbon with $ZrO_2$ in the carbothermal reduction process.

3.3 Mechanical property of the prepared C/C–ZrC composites

The flexural strength and modulus of the composites were about 93.9±7.5 MPa and 12.6±2.3 GPa, respectively. The bending strength was close to that of the C/C–ZrC composites prepared by PIP with a TCVI carbon matrix ( 95.7±8.3 MPa) [24] and that of the C/C–ZrC composites prepared by CLVD (95.9±8.3 MPa) [14]. However, it was lower than those of the C/C–ZrC composites prepared by CLVD (103.5±6.9 MPa) [13] and CLVD+PIP (154.1±9.2 MPa) [ 14]. Fig. 5(a) shows a typical stress-strain curve of the obtained C/C–ZrC composites. The curve presents an initial quasi-linear elastic behavior before reaching the maximum load. After the flexural stress reach to the maximum, a step-shape change occur at first and then dropped gradually, suggesting a typical pseudo-plastic fracture behavior of the composites. The bending fracture behavior of composites largely depends on the interfacial bonding strength of carbon fibers and the matrix [25,26]. Lu et al. reported that the C/C–ZrC composites prepared by PIP and CLVD presented a brittle fracture due to a relatively strong interfacial bonding strength between fibers and matrix [13]. The fracture modes of the C/C–ZrC composites changed from the tough fracture to

the brittle fracture with increase of ZrC content, which was attributed to strong interfacial bonding caused by the reaction between ZrC precursors with carbon fiber. In this study, the C/C–ZrC composites exhibit typical pseudo-plastic fracture behavior, indicating that a proper interfacial bonding of the carbon fibers and matrix was formed in the C/C–ZrC composites by the hydrothermal deposition combined with carbothermal reduction reaction.

Fig. 5(b) presents the fracture surface of the C/C– ZrC composites after the three-point bending test. The fracture surface of the C/C–ZrC composites is coarse with lots of pulled-out carbon fibers and fiber bundles, which is consistent with the typical pseudo-plastic fracture mode from the flexural stress-strain curve. Many holes exist on the fracture surface due to the pulled-out carbon fibers from matrix (Fig. 5(c)). The fractures surface presents a stepped shape. The pulled-out fibers were rough and adhered matrix materials, indicating moderate interface bond strength between fibers and matrix. The carbon layer deposited on carbon fiber not only hinders the damage of carbon fibers during the carbothermal reduction but also serves as interface layer improve the interface bonding. Moreover, interface debonding can be found on the fracture surface, which can dissipate fracture energy during the loading process, avoiding a brittle fracture behavior. Therefore, fiber pull-out, interfacial debonding, and fibers fracture leads to a typical pseudo-plastic fracture behavior of the C/C–ZrC composites.

3.3 Ablation resistance of the C/C–ZrC composites

Fig.6(a) shows macroscopic morphology of the C/C–Zr C composites after ablation. A small ablation pit was formed in the ablation center region. A uniform grey phase was generated on the ablation brim region of the composites. The mass and linear ablation rate of the C/C–ZrC composites is $3.7 \times 10^{-3}$ g/s and $4.2 \times 10^{-3}$ mm/s,

respectively. The $ZrO_2$, ZrC and C peaks can be found in the XRD pattern of the composites after ablation, as shown in Fig. 6 (b). The ZrC peaks of the composites after ablation decrease comparing with that of the composites before ablation. It is indicated that part of ZrC in the composite was oxidized during ablation. The preferential oxidation of ZrC would absorb heat from the flame and decrease the thermal erosion of ZrC-carbon matrix [7].

Fig. 7 shows the SEM morphology and EDS analysis of ablation center in the C/C–ZrC composites. The morphology of the $90^o$ and $0^o$ nonwoven layer, as well as the fiber webs were significantly different after ablation (Fig. 7(a)). Fig. 7 (b) is a magnify image of the $90^o$ nonwoven layer (area A). Some gaps were formed in the interfaces between carbon fibers and matrix. Many holes were left due to the oxidation of carbon fibers. Furthermore, the matrix surrounding of carbon fiber presents the accumulation of spherical particles with 3~5 um in size after ablation. The EDS analysis of the area 1 reveals that the spherical particles are mainly composed of C as well as small amount of Zr and O (Fig. 7 (e)). The cross section of carbon fiber lack of protection of ZrC. Fig. 7 (c) is a magnified image of the $0^o$ nonwoven layer (area B). The carbon fibers are ablated into needle-shaped and the ablated matrix is coarse with many pits. The $ZrO_2$ generated from the oxidation of matrix was blown away under high velocity flame and hardly form continuous oxide layer for the protection of carbon fibers. Fig. 7 (d) is a magnified image of the fiber webs (area C). A large amount of ablation product can be formed on the ablation surface due to more ZrC in the fiber webs. The ablation products contain elements of C, O, and Zr (Fig. 7 (f)), which demonstrates that the ablation products are $ZrO_2$. The oxidation of ZrC can absorb heat from the flame, leading to reduced erosion of the C/C–ZrC composites in the ablation center. In addition, $ZrO_2$ glass layer can be found

on the surface, which can effectively prevent the diffusion of oxidizing substances, acting as an ablation resistance layer for the composite.

Fig. 8 shows the SEM morphology of ablation brim region of the C/C–ZrC composites. The surface of the composites presents a coarse microstructure because of the formation of $ZrO_2$ from the oxidation of matrix and the spraying product from the ablation center (Fig. 8(a)). The magnified image of Area 1 showed that roughened spherical particles are formed on the ablation surface (Fig. 8(b)). The spherical particles are bonded to each other and form a continuous structure (Fig. 8(c)). These spherical particles results from the spherical carbon formed form hydrothermal carbonization of biomass [27, 28]. Furthermore, the surface of spherical particles presents continuous skeleton layer rather than molten states (inset of Fig. 8(c)). The EDS analysis of the area 3 displays the roughened spherical particles contains C, O, and Zr elements (Fig. 8(e)). In the ablation brim region, the temperature and gas pressure is much lower than that in the ablation center. The formed $ZrO_2$ particles after ablation are difficult to melt and form the molten layer. Therefore, most of the formed $ZrO_2$ particles are peeled off due to the weak viscosity and cause the formation of skeleton layer. It probably contain C-ZrC-$ZrO_2$ demonstrates that the roughened spherical particles phases in ablation brim region. The continuous C-ZrC-$ZrO_2$ skeleton layer was also formed on the surface of carbon fiber, as shown in Fig. 8(d). The preferential oxidation of ZrC plays an important role in the ablation brim region, which can consume oxidizing atmosphere and absorb heat from the flame, leading to reduction in material ablation. Moreover, the continuous C-ZrC-$ZrO_2$ skeleton layer generated from the oxidation of ZrC can reduce heat transfer and oxygen transport to the underlying material, as a thermal barrier material to protect the C/C–ZrC composites from erosion.

## 4. Conclusions

C/C–ZrC composites were prepared by hydrothermal de position combined with carbothermal reduction. Sub-micron ZrC particles were uniformly introduced into the nonwoven layer and fiber webs due to good permeability of the precursor solution under hydrothermal condition. The flexural strength of the C/C–ZrC composites was about 93.9±7.5 MPa and presented a typical pseudo-plastic fracture behavior. The mass and linear ablation rates of the composites were $3.7\times10^{-3}$g/s and $4.2\times10^{-3}$ mm/s under oxyacetylene ablation, respectively. The oxidation of ZrC, formation of $ZrO_2$ glass layer in ablation center and continuous C–ZrC –$ZrO_2$ skeleton layer in ablation brim region could effectively decrease the erosion of the C/C–ZrC composites during ablation. The C/C–ZrC composites prepared by hydrothermal deposition combined with carbothermal reduction present a promising potential as resistance ablation materials.

## Acknowledgements

This research was supported by National Natural Science Foundation of China [grant numbers 51402177, 51302160]; Natural Science Foundation of Education Department of Shaanxi Provincial Government [grant number 14JK1103]; and the doctoral scientific research foundation of Shaanxi University of Science & Technology [grant number BJ14-15].

## References

[1] S.F. Tang, C.L. Hu, Design, Preparation and Properties of Carbon Fiber Reinforced Ultra-High Temperature Ceramic Composites for Aerospace Applications: A Review, J. Mater. Sci. Technol. 33(2017)117-130.

[2] X.C. Jin, X.L. Fan, C.S. Lu, T.J. Wang, Advances in oxidation and ablation resistance of high and ultra-high temperature ceramics modified or coated

carbon/carbon composites, J. Eur. Ceram. Soc. 38(2018)1-28.

[3] W.Y. Wang, Q.G. Fu, B.Y Tan, Effect of in-situ grown SiC nanowires on the mechanical properties of HfC-$ZrB_2$-SiC modified C/C composites, J. Alloys Compd. 726(2017)866-874.

[4] Y. Liu, Q.G. Fu, Y.W. Guan, B.B Wang, Q.L. Shen, Ablation behavior of sharp-shape C/C-SiC-$ZrB_2$ composites under oxyacetylene flame, J. Alloys Compd. 713 (2017) 19-27.

[5] Z.H Hao, W. Sun, X. Xiong, Z.K. Chen, Y.L. Wang, Y.B. Chang, Y.L Xu, Microstructure and ablation properties of a gradient Cf/C -$XSi_2$-SiC(X = Mo,Ti) composite fabricated by reactive melt infiltration, J. Eur. Ceram. Soc.36 (2016) 3775-3782.

[6] X.T. Shen, K.Z. Li, H.J. Li, H.Y. Du, W.F. Cao, F.T. Lan, Microstructure and ablation properties of zirconium carbide doped carbon/carbon composites, Carbon .48 (2010) 344-351.

[7] C.Y. Li, K.Z. Li, H.J. Li, H.B. Ouyang, Y.L. Zhang, L.J. Guo, Ablation resistance and thermal conductivity of carbon/carbon composites containing hafnium carbide, Corros. Sci. 75 (2013) 169–175.

[8] A. Paul, S. Venugopal, J.G.P. Binner, B. Vaidhyanathan, A.C.J. Heaton, P.M. Brown, UHTC–carbon fibre composites: Preparation, oxyacetylene torch testing and characterization, J. Eur. Ceram. Soc. 33 (2013) 423-432.

[9] C.L. Hu, S.Y. Pang, S.F. Tang, Y.C. Wang, H.M. Cheng, An integrated composite with a porous Cf/C-$ZrB_2$-SiC core between two compact outer layers of Cf/C-$ZrB_2$-SiC and Cf/C-SiC, J. Eur. Ceram. Soc. 35 (2015) 1113-1117.

[10] Y. Li, S.A. Chen, X. Ma, H.F. Hu, Y. Zhang, Influence of preparation temperature on the properties of C/ZrC composites, J. Alloys Compd. 690 (2017) 206-211.

[11] M.Y. Zhang, K.Z. Li, X.H Shi, L.J. Guo, J.J. Sun, Q.L. Shen, Effects of low-temperature thermal cycling treatment on the microstructures, mechanical properties and oxidation resistance of C/C-ZrC-SiC composites, J. Alloys Compd. 721 (2017)28-35.

[12] X. Yang, Q.Z. Huang, Z.A. Su, X. Chang, L. Xue, P. Zhong, J. Li, Ablative property and mechanism of C/C-$ZrB_2$-ZrC-SiC composites reinforced by SiC networks under plasma flame, Corros. Sci. 107 (2016) 9-20.

[13] J.H. Lu, Q.C. He, Y.W. Wang, H.J. Li, Q.G. Fu, Preparation of co-deposited C/C-ZrC composites by CLVD process and its properties, J. Alloys Compd. 686 (2016) 823-830.

[14] Q.C. He, J.H. Lu, Y.W. Wang, C.C. Wang, Effects of joint processes of CLVD and PIP on the microstructure and mechanical properties of C/C-ZrC composites, Ceram. Int. 42(2016)17429-17435.

[15] C.Y. Li, K.Z. Li, H.J. Li, H.B. Ouyang, et al. Effect of $ZrO_2$ morphology on the ablation resistance of carbon/carbon composites containing ZrC prepared by the carbothermal reduction reaction. Corros. Sci. 102(2016) 405-412.

[16] H.B. Ouyang, C.Y. Li, J.F. Huang, J. Fei, Synthesis of carbon/carbon composites by hydrothermal carbonization using starch as carbon source, RSC Adv. 4(2014)12586-12589.

[17] L.Y. Cao, Z. Bai, J.F. Huang, H.B. Ouyang, J.P. Wu, Ablation properties of Cf/C-SiC-$MoSi_2$ composites: Effects of hydrothermal penetration temperature, J. Alloys Compd.703 (2017) 45-55.

[18] S. Sagadevan, J Podder, I Das, Hydrothermal synthesis of zirconium oxide nanoparticles and its characterization, J. Mater. Sci: Mater. Electron. 27(2016)5622-5627.

[19] J.A. Darr, J.Y. Zhang, N.M. Makwana, X.L. Weng, Continuous Hydrothermal Synthesis of Inorganic Nanoparticles: Applications and Future Directions, Chem. Rev. 117 (2017)11125-11238.

[20] Y. Gao, J.T. Ma, X.Y. Zhao, S.C. Hao, C.S. Deng, B. Liu, The Fabrication of $ZrO_2$-ZrC Microspheres by Internal Gelation and Carbothermal Reduction Process, J. Am. Ceram. Soc. 99(2016)1184-1191.

[21] C.L. Yan, R.J. Liu, C.R. Zhang, Y.B. Cao, X.H Long, Synthesis of $ZrB_2$ Powders from $ZrO_2$, BN, and C, J. Am. Ceram. Soc. 99(2016)16-19.

[22] K.Z. Li, X. Jing, Q.G. Fu, H.J. Li, L.J. Guo, Effects of porous C/C density on the densification behavior and ablation property of C/C-ZrC-SiC composites, Carbon. 57(2013)161-168.

[23] Y.M. Li, Y.S. Hu, Hong Li, L.Q. Chen, X.J. Huang, A superior low-cost amorphous carbon anode made from pitch and lignin for sodium-ion batteries, J. Mater. Chem. A. 4(2016)96-104.

[24] J. Xie, K.Z. Li, G.D. Sun, H. Li, Effects of precursor concentration on the microstructure and properties of ZrC modified C/C composites prepared by precursor infiltration and pyrolysis, Ceram. Int. 43(2017)14642-14651.

[25] C.H. Ma, L.J. Guo, H.J. Li, W.L. Tan, T. Duan, N.K. Liu, M.Y. Zhang, Effects of high-temperature annealing on the microstructures and mechanical properties of C/C-ZrC-SiC composites prepared by precursor infiltration and pyrolysis, Mater. Design. 90 (2016) 373-378.

[26] D.K. Wang, S.M. Dong, H.J. Zhou, Y.M. Kan, Z. Wang, G.X. Zhu, X.W. Chen, Y.P. Cao, Effect of pyrolytic carbon interface on the properties of 3D C/ZrC-SiC composites fabricated by reactive melt infiltration, Ceram. Int. 42(2016)10272-10278.

[27] A. Jain, R. Balasubramanian, M.P. Srinivasan, Hydrothermal conversion of biomass waste to activated carbon with high porosity: A review, Chem. Eng. J. 283(2016)789-805.

[28] H.Y. Zhao, X.A. Lu, Y. Wang, B. Sun, X.H. Wu, H.F. Lu, Effects of additives on sucrose-derived activated carbon microspheres synthesized by hydrothermal carbonization, J. Mater. Sci. 52(2017)10787-10799.

**List of Figure Captions**

Fig.1. Schematic diagram of preparation process of the C/C–ZrC composites.

Fig. 2 SEM morphology (a) and Raman spectrum (b) of C/C porous sample.

Fig. 3 XRD pattern (a) and backscattered electron image of the cross section (b) of C/C–ZrC composites.

Fig. 4 SEM morphology of nonwoven layer in C/C–ZrC composites (a), (b) is the magnified micrographs of $90^{o}$ nonwoven layer (area 1), (c) is the backscattered electron image of (b), (d) is the magnified micrographs of $90^{o}$ nonwoven layer (area 2), (e) is high magnification of the matrix, (f) is the magnified micrographs of $0^{o}$ nonwoven layer, (g) and (h) are the SEM morphology of fiber webs and the corresponding magnified micrographs.

Fig. 5 Flexural stress-strain curve (a), low magnification image (b) and high magnification image of fracture surface of the C/C– ZrC composites.

Fig. 6 Macroscopic morphology (a) and XRD pattern (b) of the C/C–ZrC composite after ablation.

Fig. 7 SEM morphology of ablation center of the C/C–ZrC composites (a), (b) and (c) are the magnified images of the $90^{o}$ and $0^{o}$ nonwoven layer (area A and B), respectively, (d) is the magnified image of the fiber webs (area C), (e) and (f) are EDS analysis of area 1 and 2, respectively.

Fig. 8 SEM morphology of ablation brim region of the C/C–ZrC composites (a), the magnified images of area 1 (b) and (c), the magnified image of area 2 (d), EDS analysis of area 3.

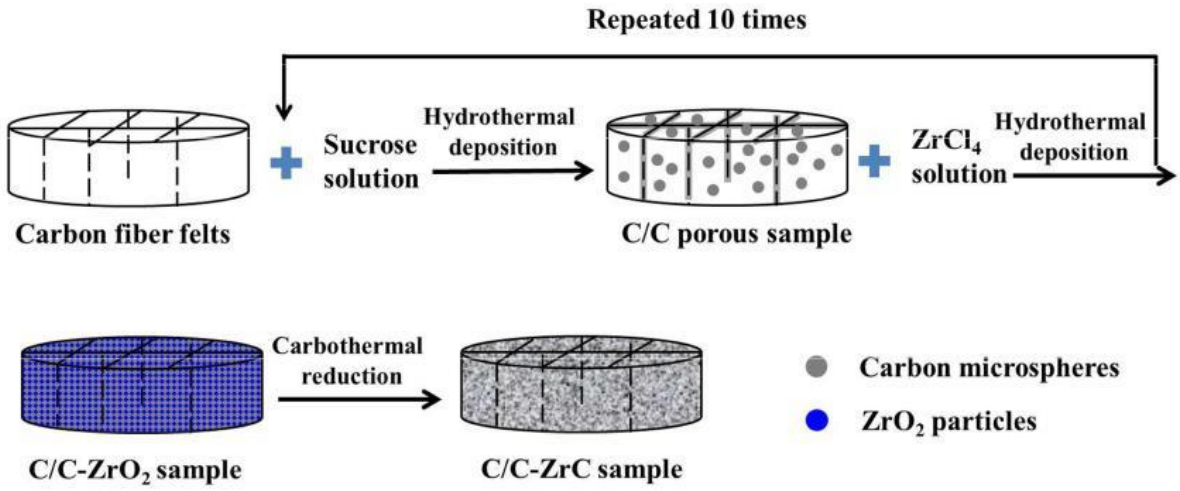
Repeated 10 times
Carbon fiber felts
Sucrose solution
Hydrothermal deposition
C/C porous sample
$ZrCl_4$ solution
Hydrothermal deposition
$C/C-ZrO_2$ sample
Carbothermal reduction
C/C-ZrC sample
Carbon microspheres
$ZrO_2$ particles

Figure 1

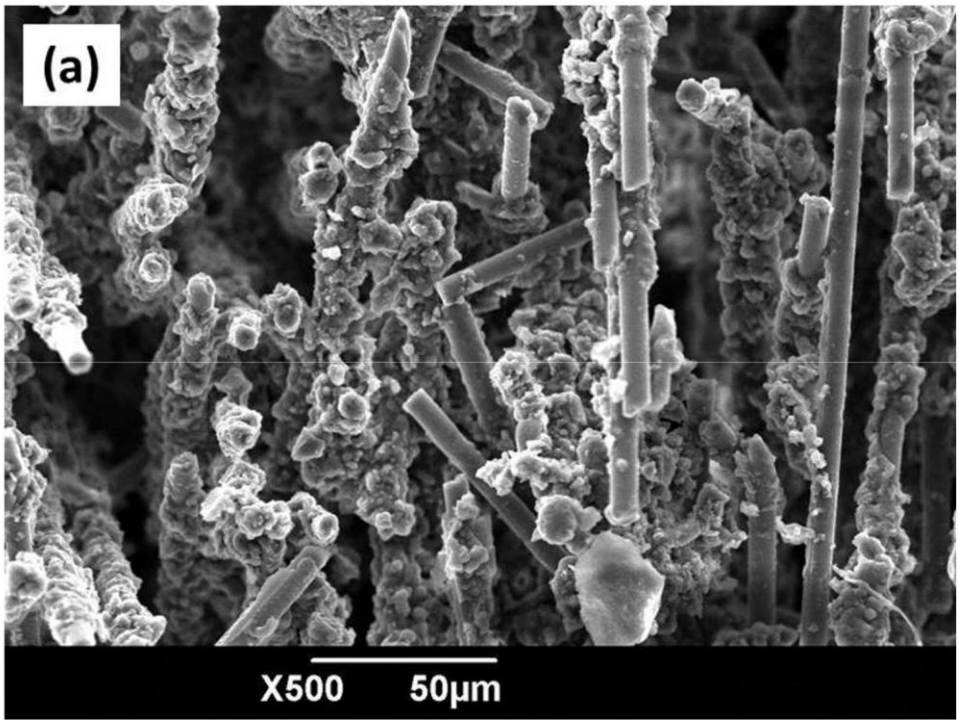
(a)
X500
50μm

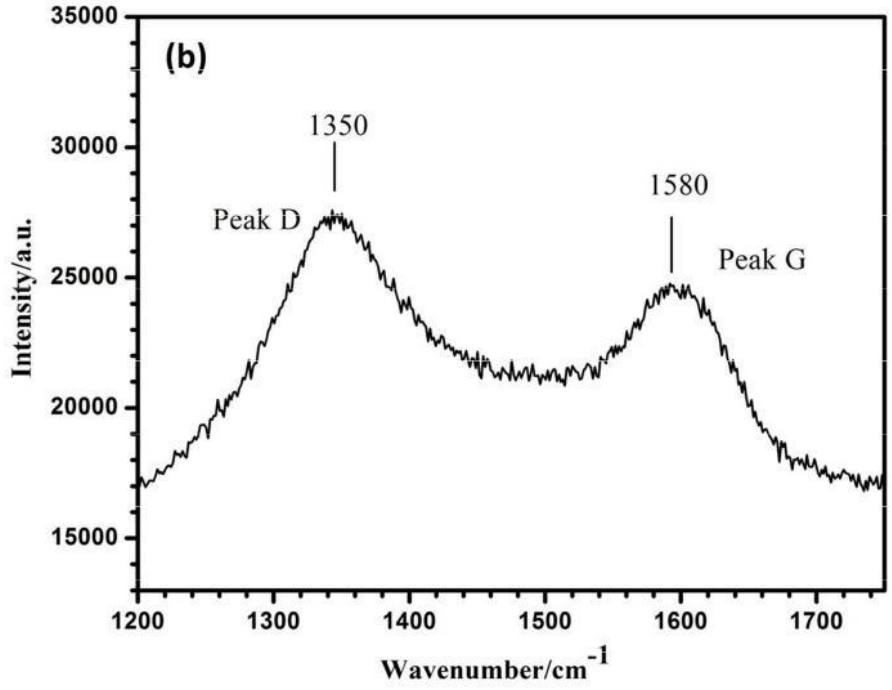
(b)
1350
Peak D
1580
Peak G
Intensity/a.u.
35000
30000
25000
20000
15000
1200
1300
1400
1500
1600
1700
Wavenumber/cm-1

Figure 2

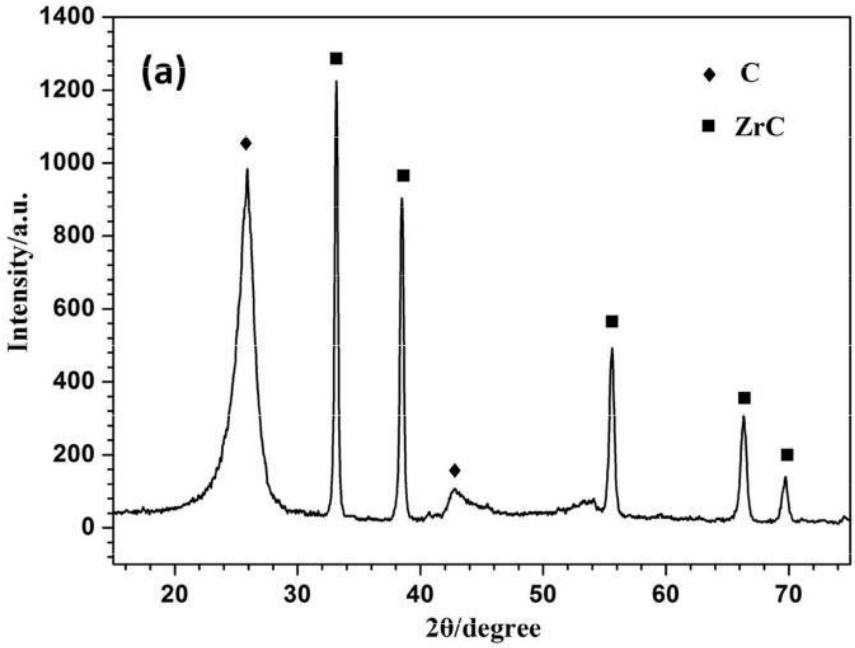
(a)
C
ZrC
Intensity/a.u.
2θ/degree
1400
1200
1000
800
600
400
200
0
20
30
40
50
60
70

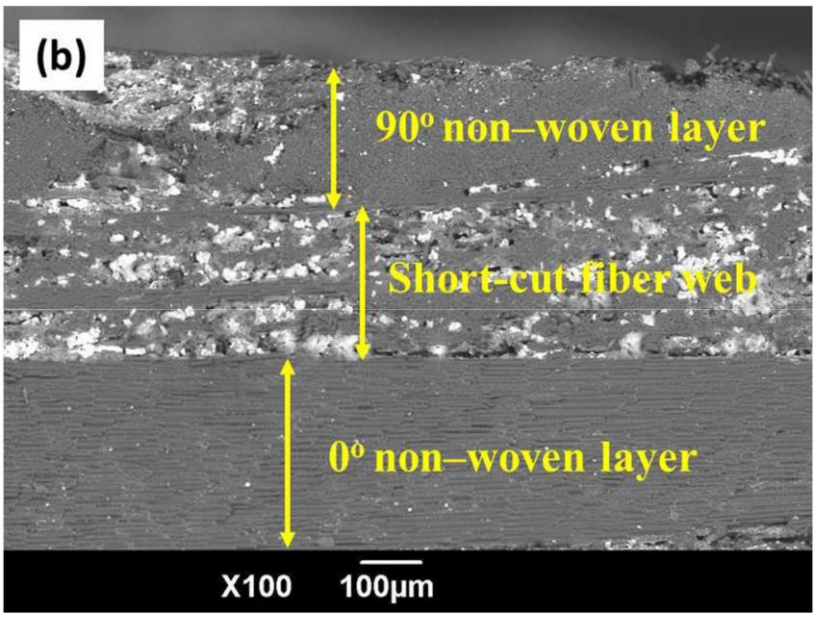
(b)
90° non–woven layer
Short-cut fiber web
0° non–woven layer
X100
100μm

Figure 3

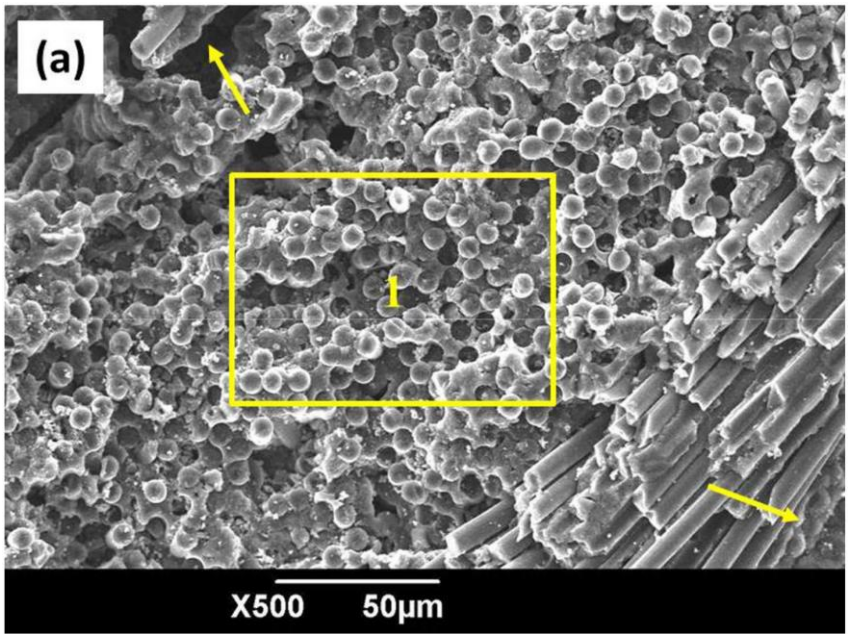
(a)
1
X500
50μm

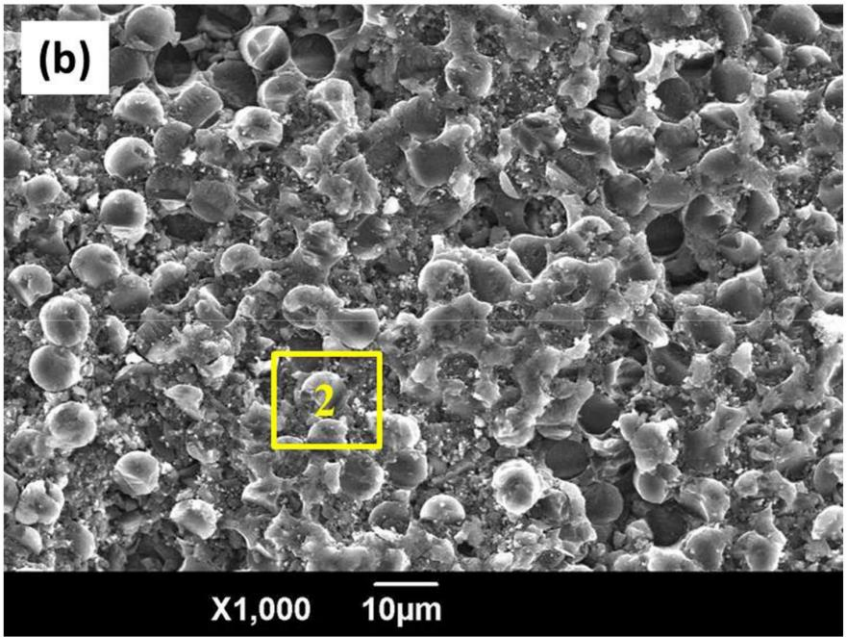
(b)
2
X1,000
10μm

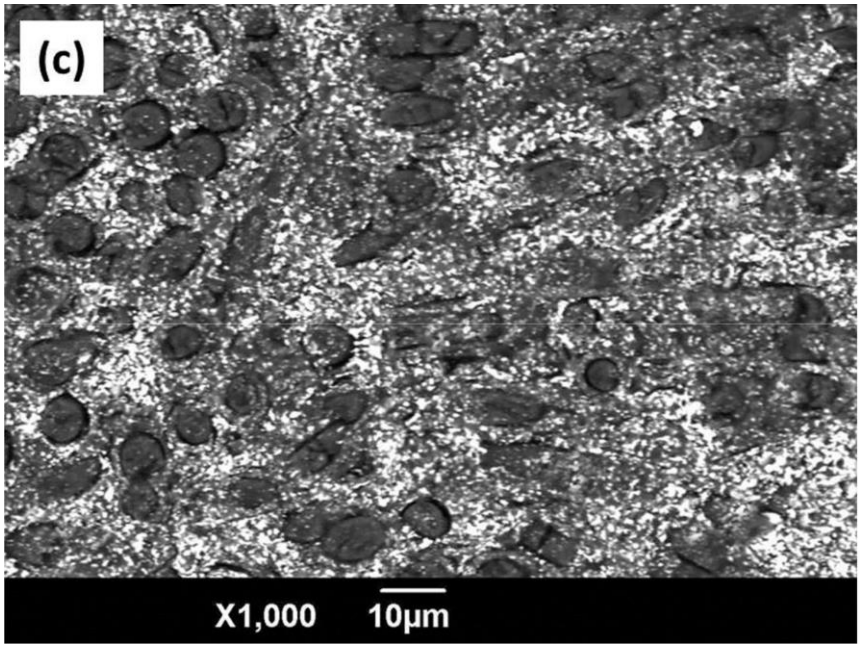
(c)
X1,000
10μm

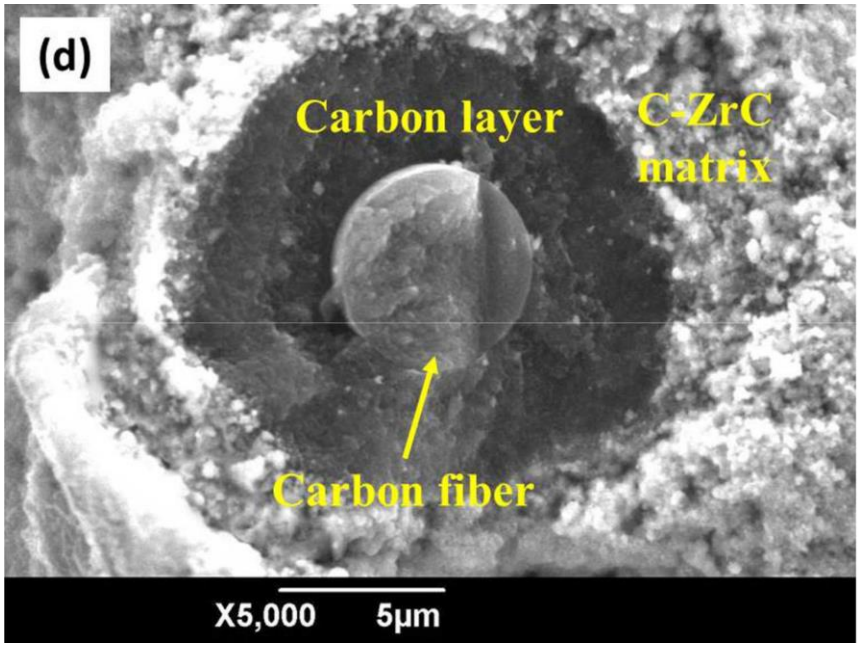
(d)
Carbon layer
C-ZrC
matrix
Carbon fiber
X5,000
5μm

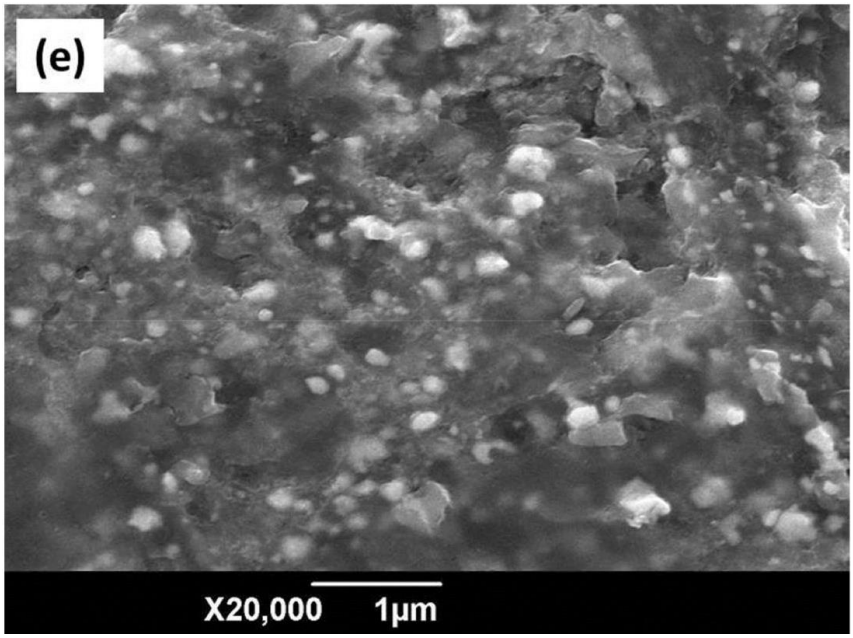
(e)
X20,000
1μm

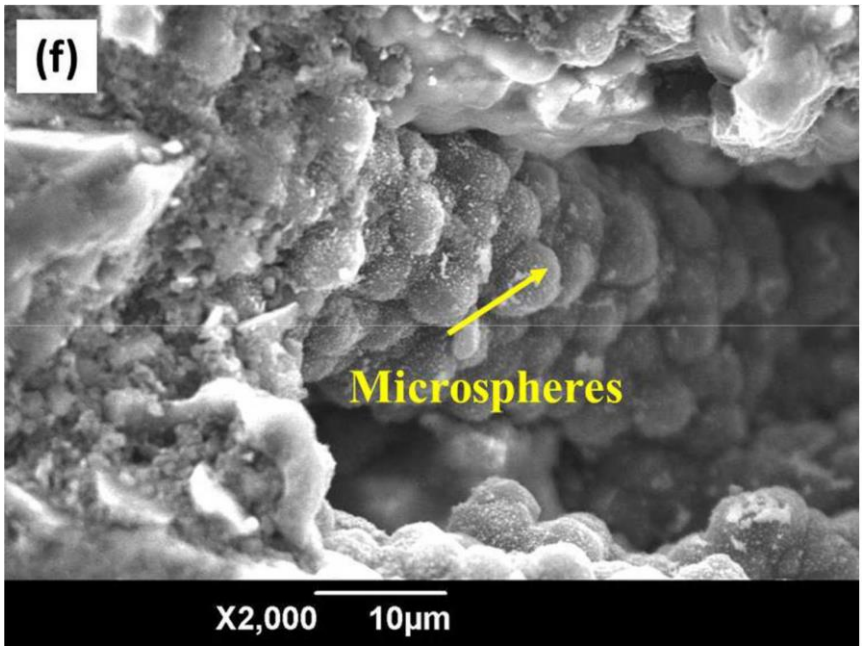
(f)
Microspheres
X2,000
10μm

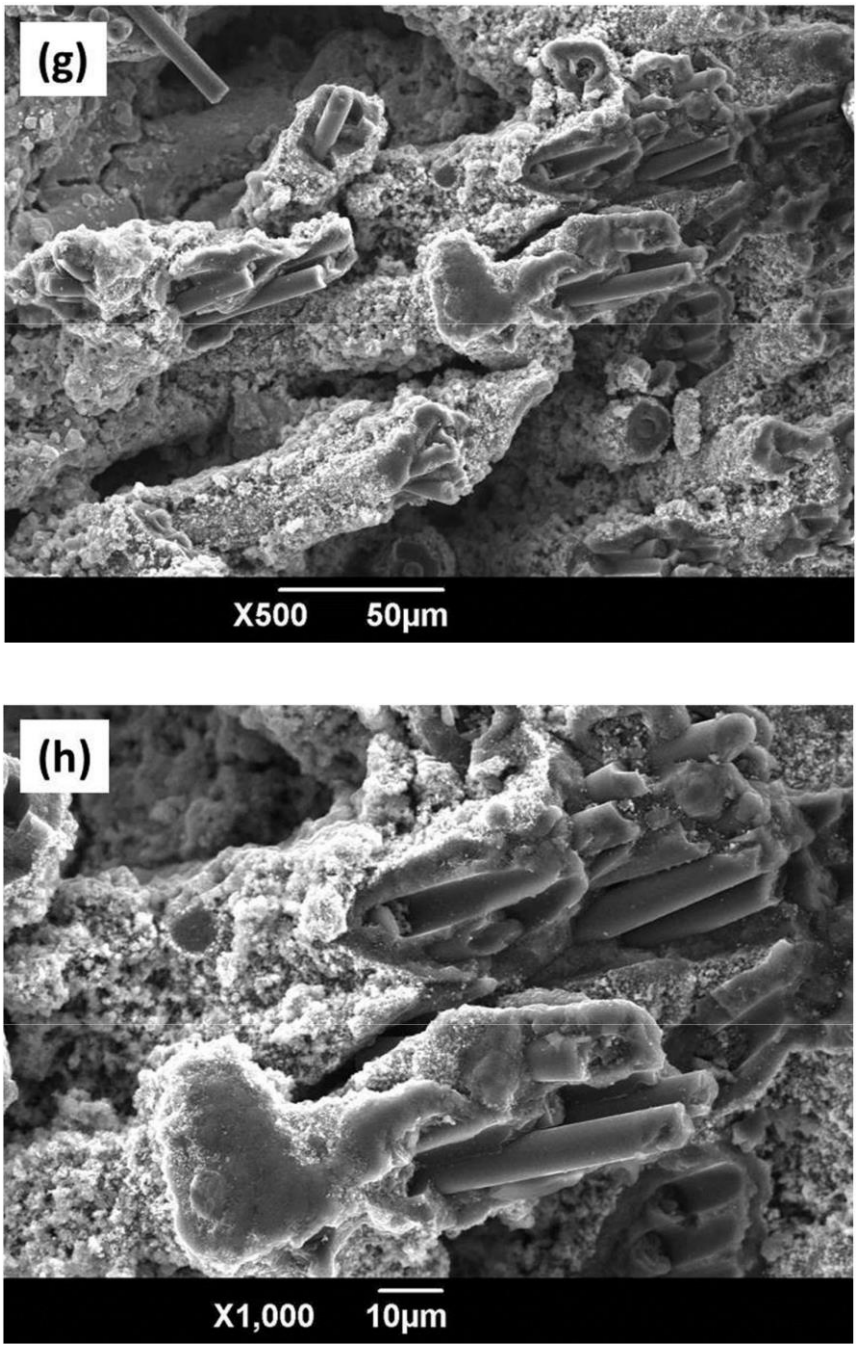


Figure 4

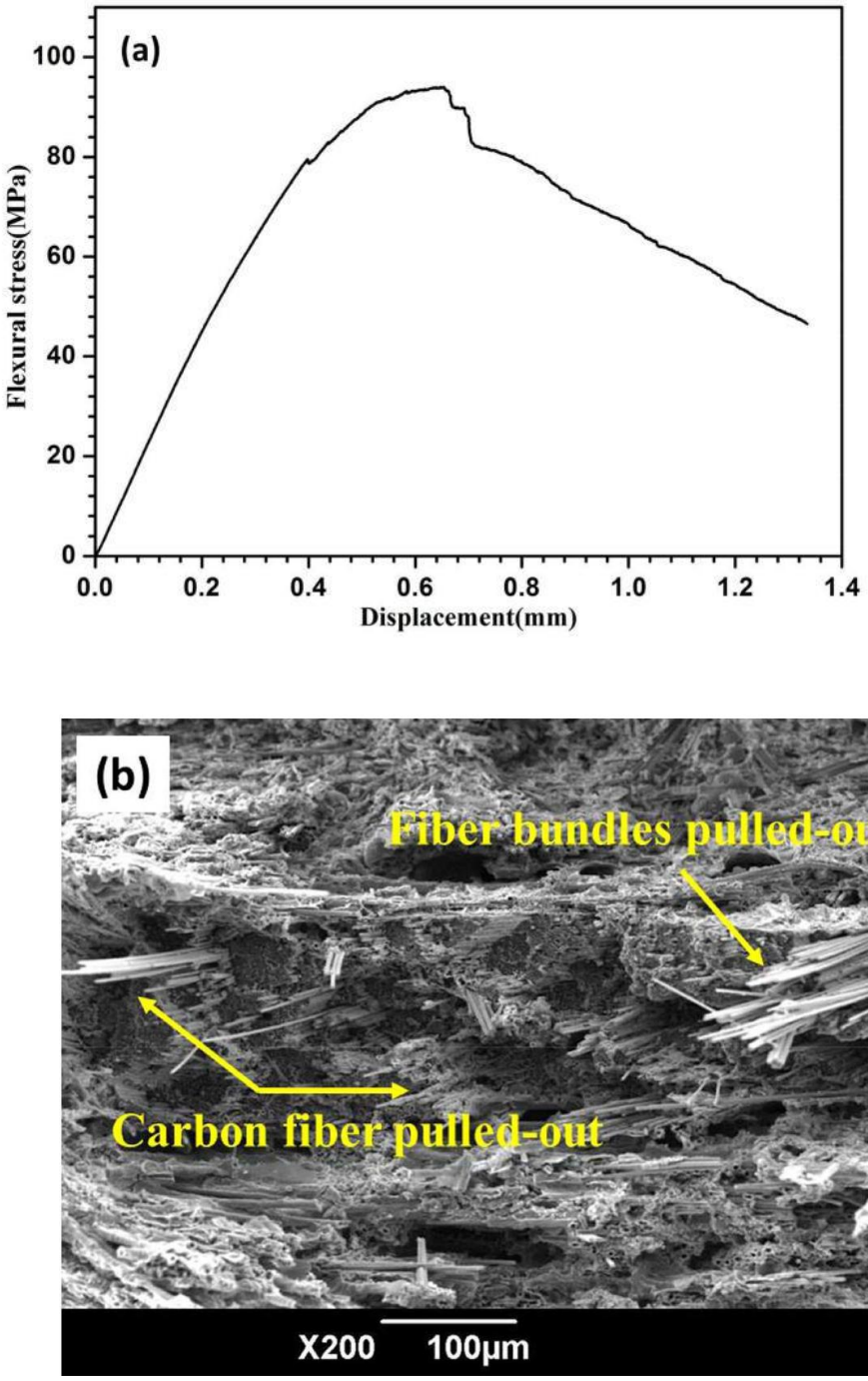
(a)
Flexural stress(MPa)
Displacement(mm)
0
20
40
60
80
100
0.0
0.2
0.4
0.6
0.8
1.0
1.2
1.4
(b)
Fiber bundles pulled-out
Carbon fiber pulled-out
X200
100μm

Figure 5

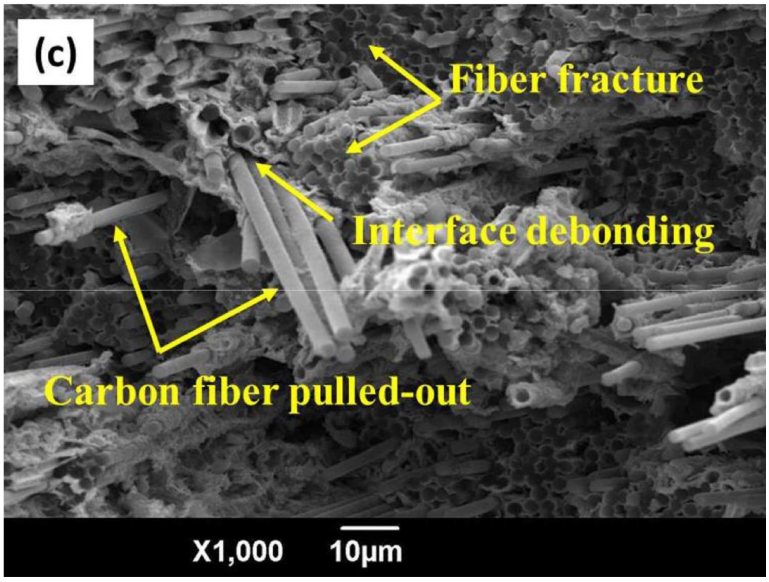
(c)
Fiber fracture
Interface debonding
Carbon fiber pulled-out
X1,000
10μm

Figure 5

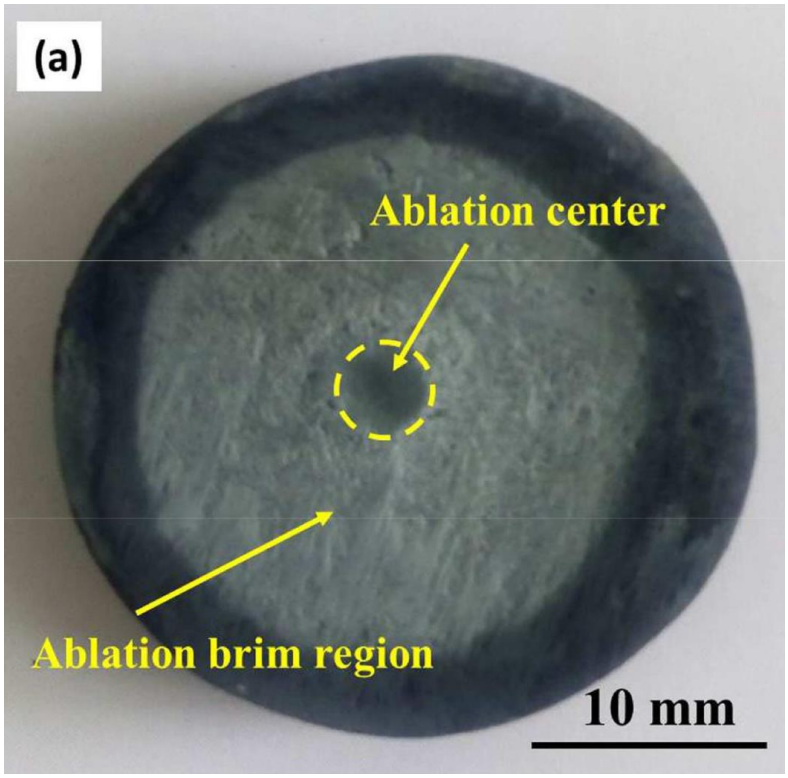
(a)
Ablation center
Ablation brim region
10 mm

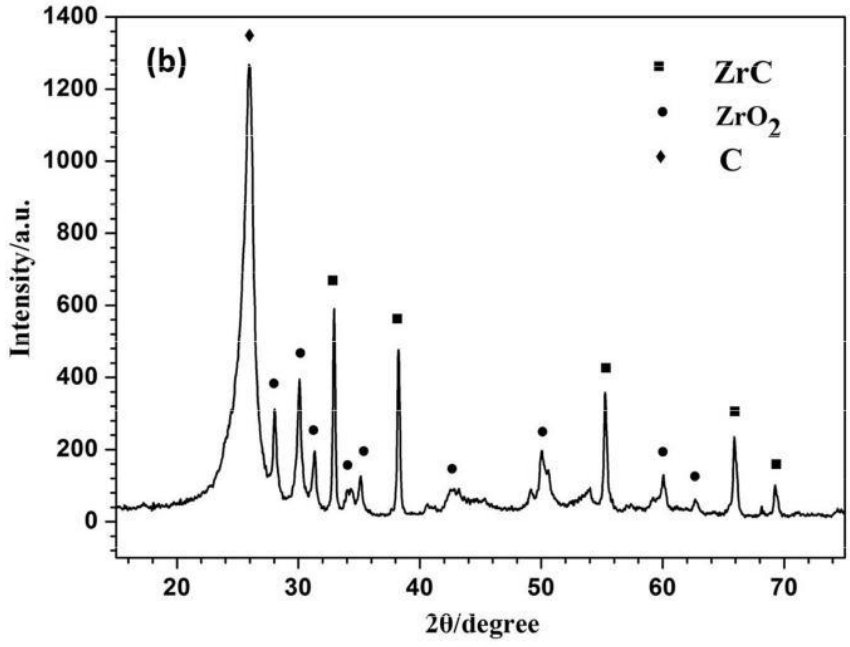
(b)
ZrC
ZrO2
C
Intensity/a.u.
2θ/degree
0
200
400
600
800
1000
1200
1400
20
30
40
50
60
70

Figure 6

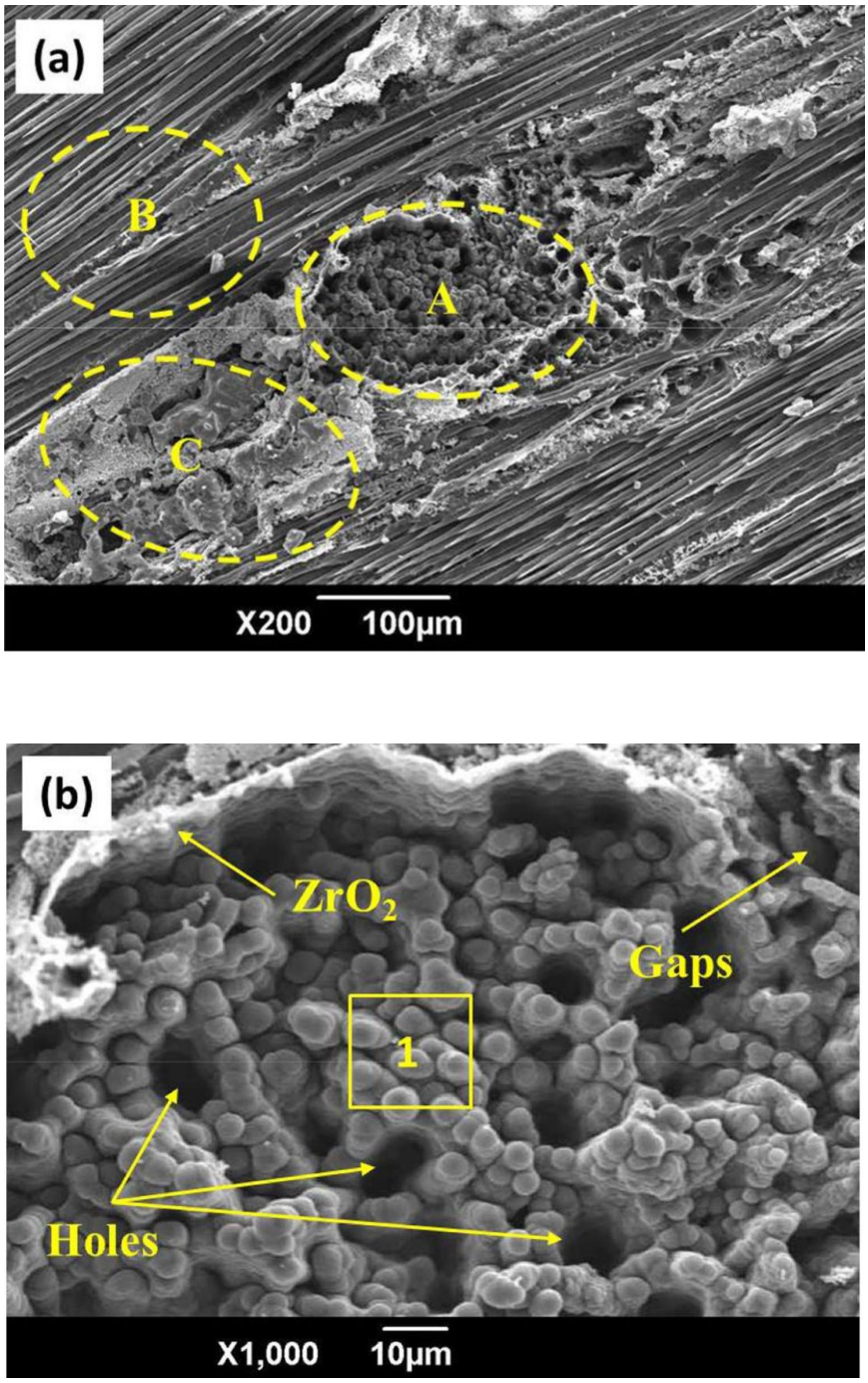


Figure 7

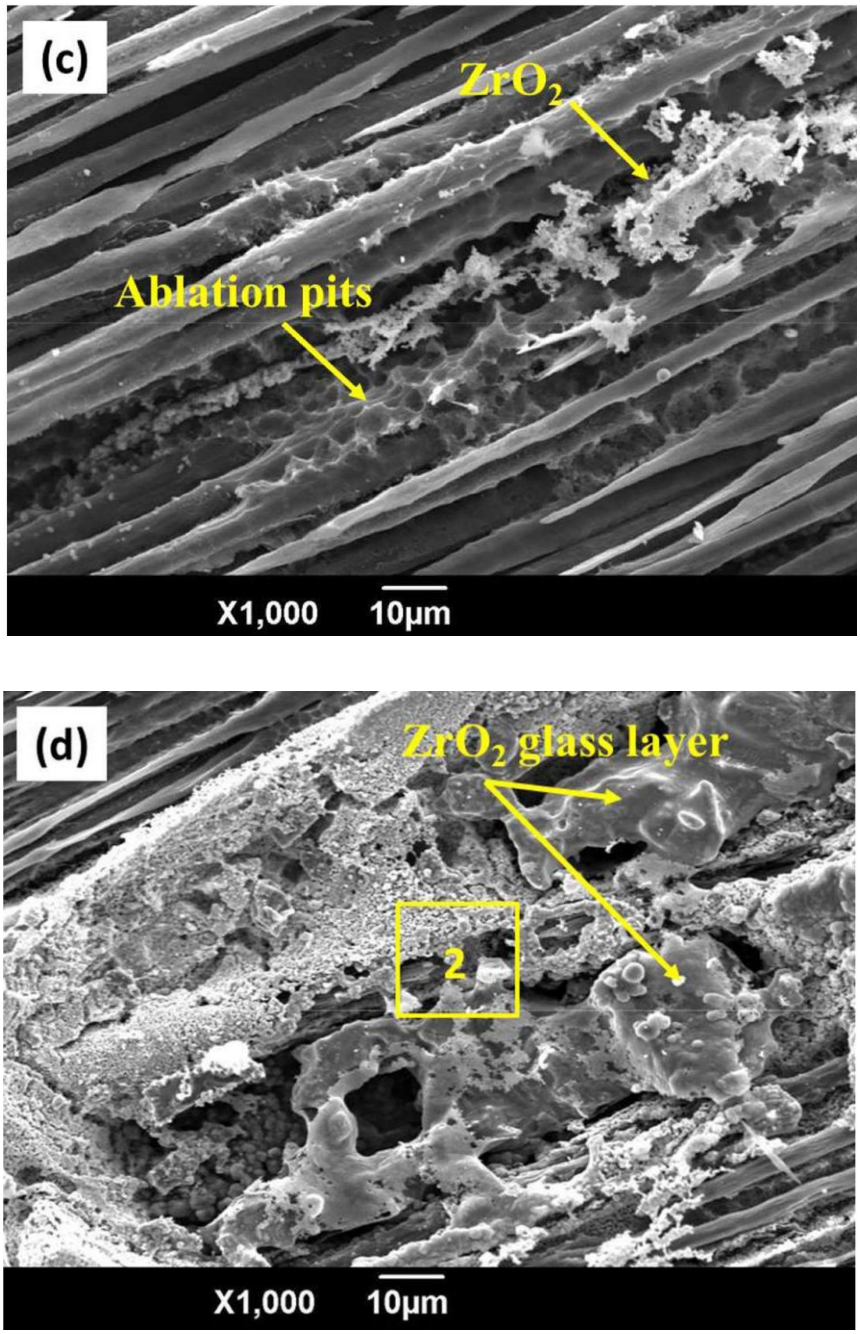
(c)
$ZrO_2$
Ablation pits
X1,000
10μm
(d)
$ZrO_2$ glass layer
2
X1,000
10μm

Figure 7

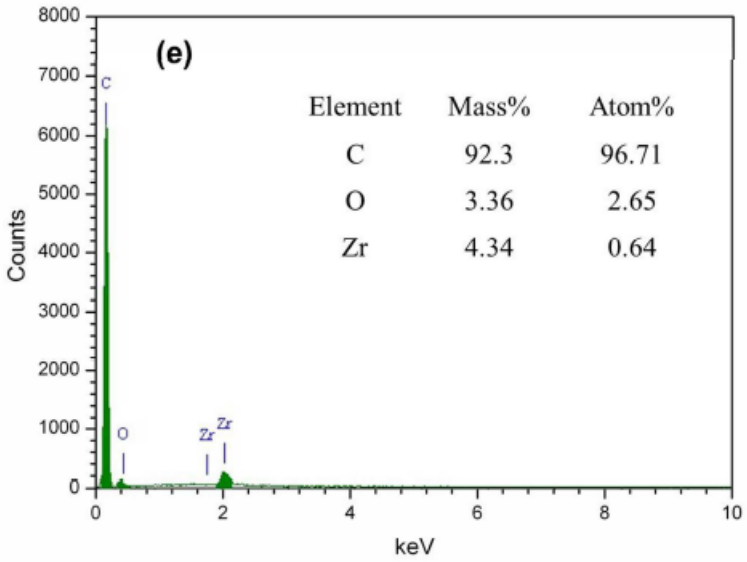
(e)
Element Mass% Atom%
C 92.3 96.71
O 3.36 2.65
Zr 4.34 0.64
Counts
keV
C
O
Zr
Zr

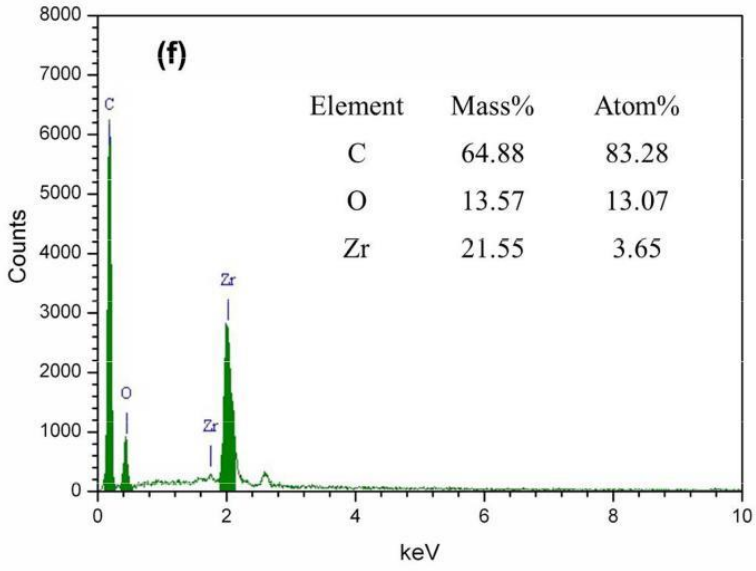
(f)
Element Mass% Atom%
C 64.88 83.28
O 13.57 13.07
Zr 21.55 3.65
Counts
keV
C
O
Zr
Zr

Figure 7

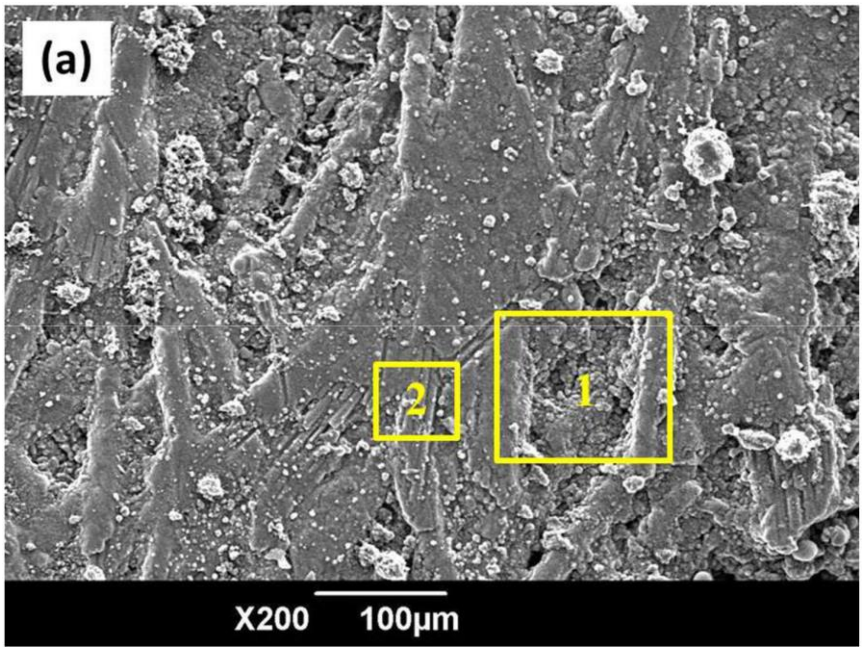
(a)
2
1
X200
100μm

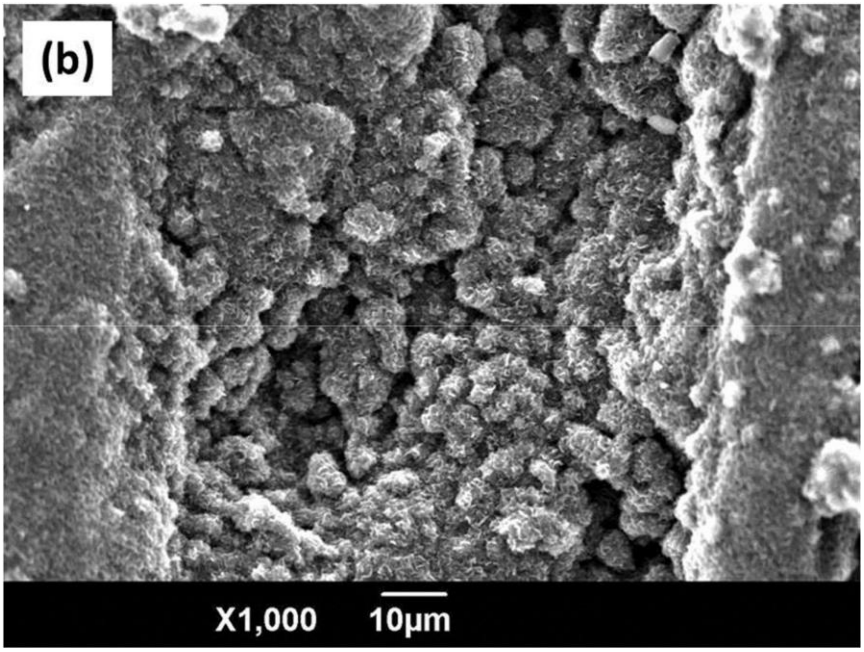
(b)
X1,000
10μm

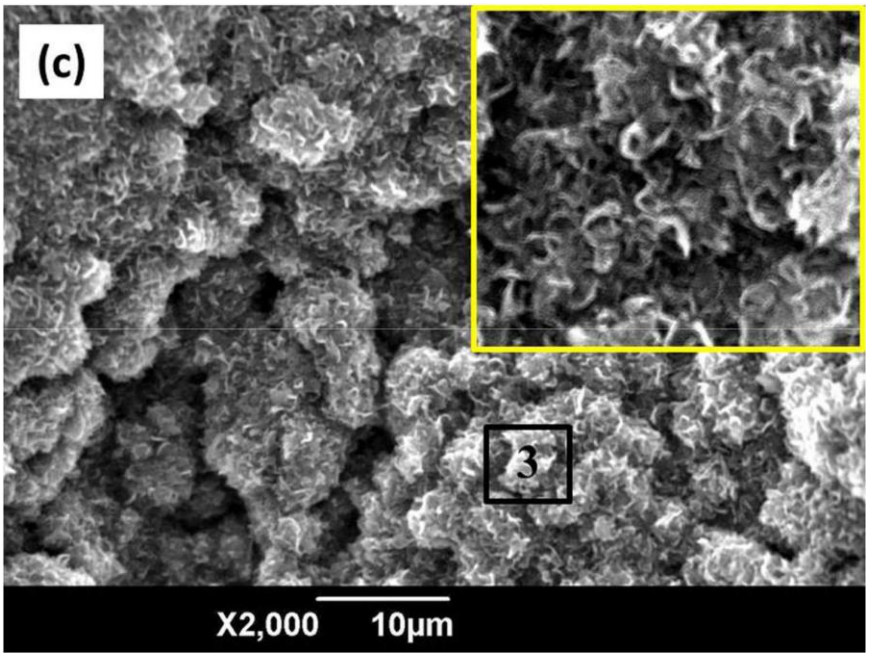


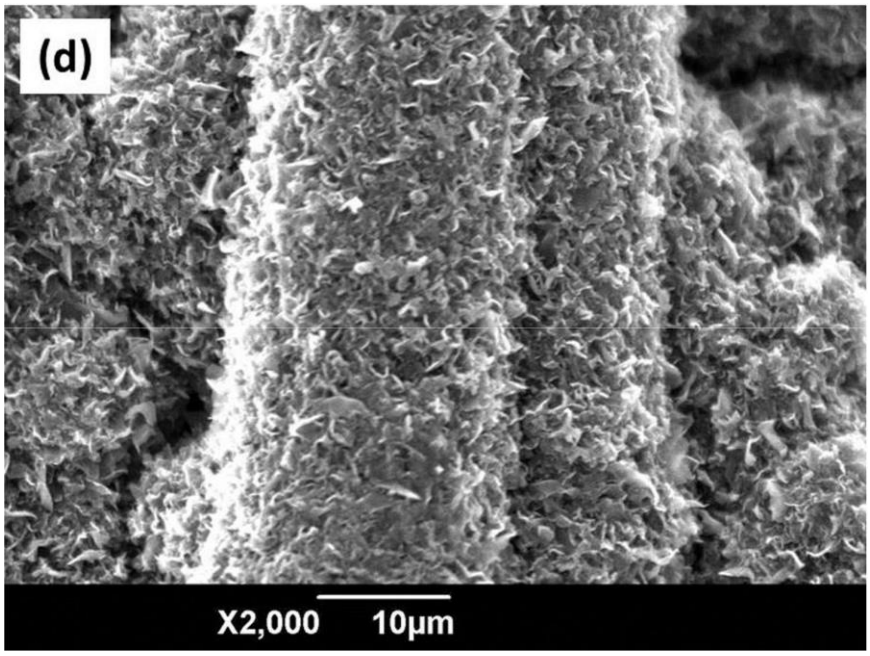


Figure 8

Figure

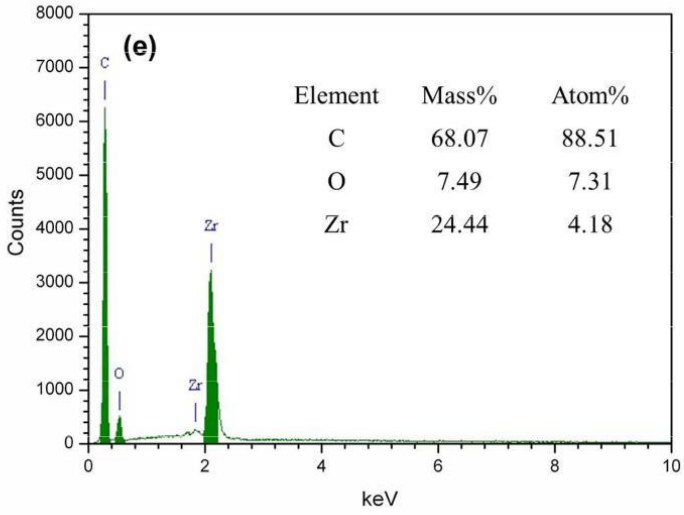


Figure 8